Marriage Strategy of Structure and Composition Designs for Intensifying Ultrasound & MR & CT Trimodal Contrast Imaging

Kun Zhang,[†,‡,§] Hangrong Chen,*,[‡] Pei Li,[†,§] Xiaowan Bo,[†,§] Xiaolong Li,[†,§] Zeng Zeng,[†,§] and Huixiong Xu*,[†,§]
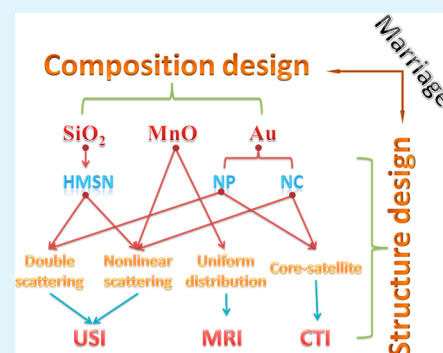
[†]Department of Medical Ultrasound, Shanghai Tenth People's Hospital, and [§]Thyroid Institute, Tongji University School of Medicine, 301 Yan-chang-zhong Road, Shanghai, 200072, P. R. China

[‡]State Key Laboratory of High Performance Ceramics and Superfine Microstructures, Shanghai Institute of Ceramics, Chinese Academy of Sciences, 1295 Ding-Xi Road, Shanghai 200050, P. R. China

Ⓢ Supporting Information

ABSTRACT: Despite great efforts having been devoted to the design of multimodal imaging probe, almost all design principles of nanotheranostic agents subordinate to simple assemblies of building blocks, resulting in complex preparation process and discounted ability, that is, $1 + 1 < 2$. In this report, a novel design strategy, marriage of structure design and composition design that can maximize imaging ability of each building block, ultimately achieving $1 + 1 \geq 2$, has been established. Moreover, a high-efficient ultrasound (US) & MR & CT trimodal contrast agent acts as model to instantiate this design strategy, wherein nanoparticles-induced nonlinear scattering and rattle-type structure-induced double scattering enhancing US imaging, and uniform distribution of Mn^{2+} paramagentic centers and "core−satellite" structure of Au atoms favoring enhanced MR imaging and CT imaging, respectively have been validated, achieving optimization of structure design. Importantly, the selected components, silica, Au and MnO are endowed with excellent biocompatibility, displaying the marriage strategy of composition design with aforementioned structure optimization. In in vivo evaluations, such a biocompatible trimodal probe is demonstrated of excellent performance in intensifying CT, MR and US imaging in vivo, especially after positively charged modification by PEI promoting more probes retained in tumor. More importantly, as a universal design strategy, the involved principles in constructing such a US&MR&CT trimodal imaging probe promise great potentials in guiding designs of other materials-based multimodal imaging probe.

KEYWORDS: composition & structure marriage, double scattering, enhanced nonlinear scattering, uniform distribution, core−satellite, ultrasound & MR & CT trimodal imaging probe

INTRODUCTION

Early precise diagnosis for tumors, especially desirable for highly deadly and invasive cancers has increasingly gained interest, evenly outweighing cancer treatment,[1] but remains a challenging endeavor to date. Although significant advances in diagnosis approaches, e.g., X-ray computed tomography (CT), magnetic resonance (MR), ultrasound (US), the currently prevalent photoacoustic tomography (PAT), have been achieved,[2−5] any monodiagnosis failed to acquire complete information on cancers due to their inherent drawbacks, e.g., US molecular imaging can conduct real-time and deep tissue diagnosis, but it shares poor resolution.[6−9] Therefore, alliances between several appropriate imaging modalities were increasingly prevalent.[8,9] Unfortunately, despite many efforts devoted to combination of several imaging modes and organization of corresponding CAs,[10−12] the two intriguing concerns, win-win organizations of appropriate imaging modalities and according CAs' design remain challenging. In detail, owing to lack of sufficient understanding and rational cost-to-benefit analysis for each imaging approach, previous organizations of different

imaging modalities are usually arbitrary,[13−15] e.g., Liu et al. prepared multifunctional $NaYF_4$:Yb, Er@mSiO_2@Fe_3O_4−PEG nanoparticles for UCL/MR bioimaging,[15] but SiO_2 coating impeded light transmission and resulted in reduced fluorescence intensity in comparison to free UCNP nanoparticles,[16] and simultaneously owing to blockage of H_2O coordination with the inner Fe_3O_4 nanoparticles by PEG and SiO_2,[17] the T_2-weighted MRI of Fe_3O_4 was weakened in comparison to free Fe_3O_4 nanoparticles. Accordingly, the commonly used design strategy of multimodal imaging CAs merely highlights selection of active imaging component without emphasis on rational structure configuration, which usually results in discounted imaging ability of each active component relative to use alone, namely $1 + 1 < 2$.

In this report, with in depth understanding of each operation principle, ultrasound, CT, and MR are selected to acquire the

Scheme 1. Principles of Amino-Mediated SSR Strategy and Marriage of Structure Design and Composition Design: (A) Schematic Image on How to Prepare the US&MR&CT Trimodal Probe, Wherein Step 1 Is To Produce Au@HMSN/Au Nanoparticle, and in Step 2, $[MnO_4]^-$ Precursor Was Reduced into MnO by Residual Amino Groups after Step 1; (B) Detailed Schematic of How the Marriage of Structure Design and Composition Design to Improve US, MR, and CT Imaging
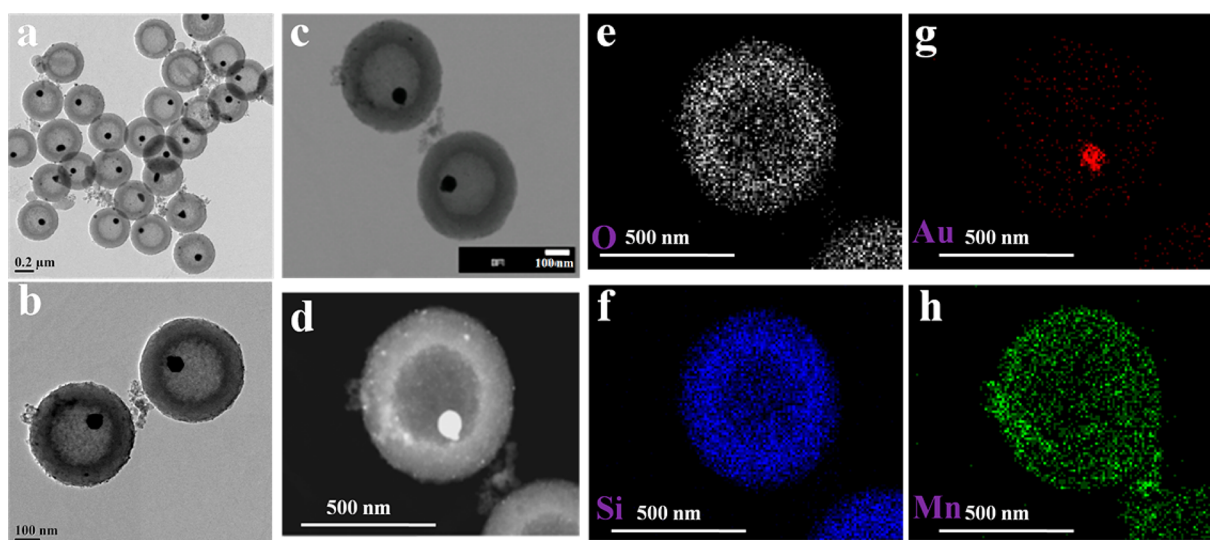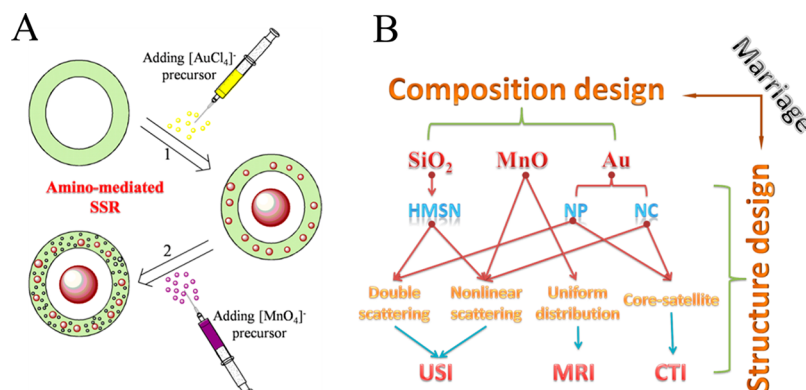

Figure 1. Characterizations on structure and morphology of such a trimodal imaging probe. (a–c) TEM images, (d) STEM image, and (e–h) element mappings of Au@HMSN/Au&MnO. It is obviously observed that a large Au nanoparticle emerged in hollow cavity of HMSN, and some smaller Au nanocrystals and large numbers of MnO nanoparticles evenly distribute in shell of HMSN.

complete information on caners via exerting their personal advantages.[18,19] Differing from the previous design strategy of CAs, namely simple assembly of building blocks, a novel design strategy, marriage of structure and composition designs, has been developed. Moreover, a sequential self-reduction reaction (SSR) synthetic approach has been well established to fabricate a biocompatible US&MR&CT "all in one" trimodal imaging probe (termed Au@HMSN/Au&MnO) (Scheme 1A) as ideal models to exemplify this novel design strategy. Such an "all in one" trimodal probe was demonstrated of considerably maximizing imaging abilities of US, MR and CT, respectively, truthfully achieving 1 + 1 > 2, as shown in Scheme 1B. In composition design, silica, Au and MnO of excellent biosafety are taken as active units of US, CT, and MR CAs in sequence. Concerning structure design, design principles of nonlinear scattering and double-scattering in a single nanoprobe are highlighted to substantially improve US imaging; uniform distribution of Mn paramagentic centers and "core–satellite" structure consisted of a large Au nanoparticle and some smaller Au nanocrystals can evidently improve MR and CT imaging, respectively. This trimodal imaging probe showed in vivo US&MR&CT enhanced imaging of VX2 tumor, especially after modification by positively charged PEI. This novel trimodal probe highlights a new avenue to intensifying clinic precise diagnosis and implementing junior pathologic evaluation.

■ RESULTS AND DISCUSSION

Preparation of Multifunctional Nanoparticle—Au@HMSN/Au&MnO. The trimodal probe, Au@HMSN/Au&MnO was prepared using a newly developed amino group-mediated sequential self-reduction reaction (SSR) strategy (Scheme 1A). Briefly, amino group-functionalized hollow mesoporous silica nanoparticles (HMSNs) were prepared via a previous method and acted as a building platform.[20,21] In Figure S1a1–a3, it is clearly found that well-distributed amino groups-functionalized HMSNs of around 400 nm in diameter were easily within reach. Afterward, depending on the reducibility of amino groups tethered to HMSNs, a large Au nanoparticle and some smaller Au nanocrystals in situ first emerged in the hollow cavity and mesoporous shell of HMSNs (named Au@HMSN/Au), respectively, followed by yielding MnO nanoparticles uniformly distributed in mesoporous shell,
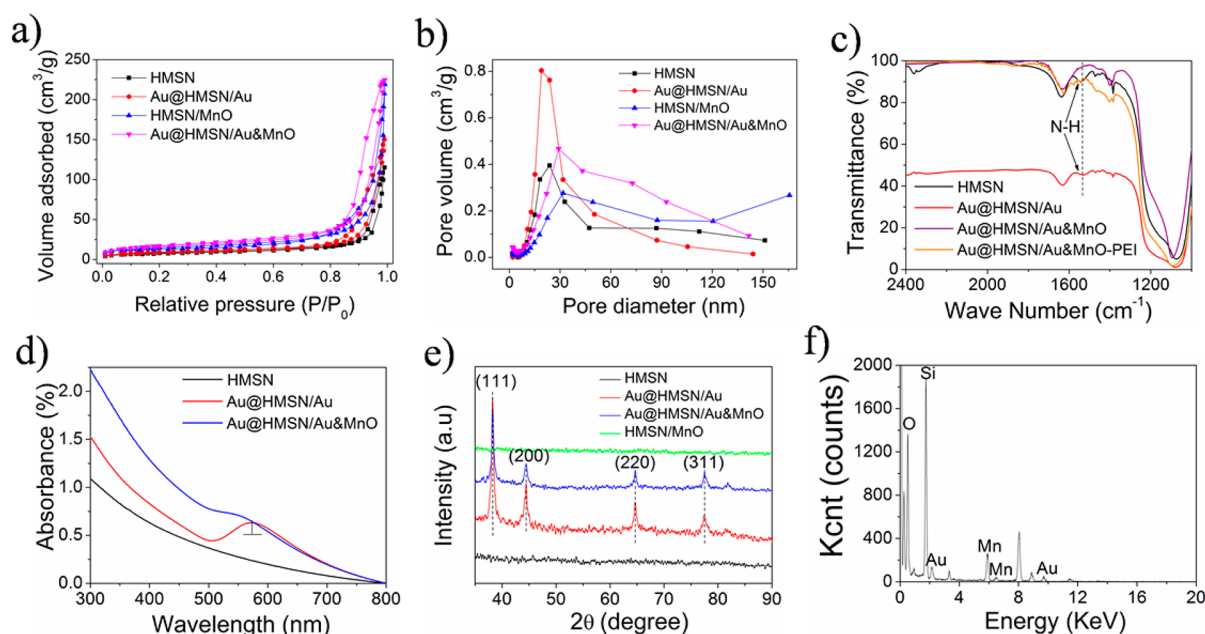
Figure 2. Analysis and characterizations of HMSNs, Au@HMSN/Au (immediate product), and Au@HMSN/Au&MnO (ultimate product). (a) N_2 desorption and desorption isotherms; (b) pore diameter distribution profiles; (c) FTIR spectral profiles; (d) UV−vis spectral profiles; (e) XRD pattern of HMSNs, Au@HMSN/Au, and Au@HMSN/Au&MnO; and (f) EDX spectrum of Au@HMSN/Au&MnO.
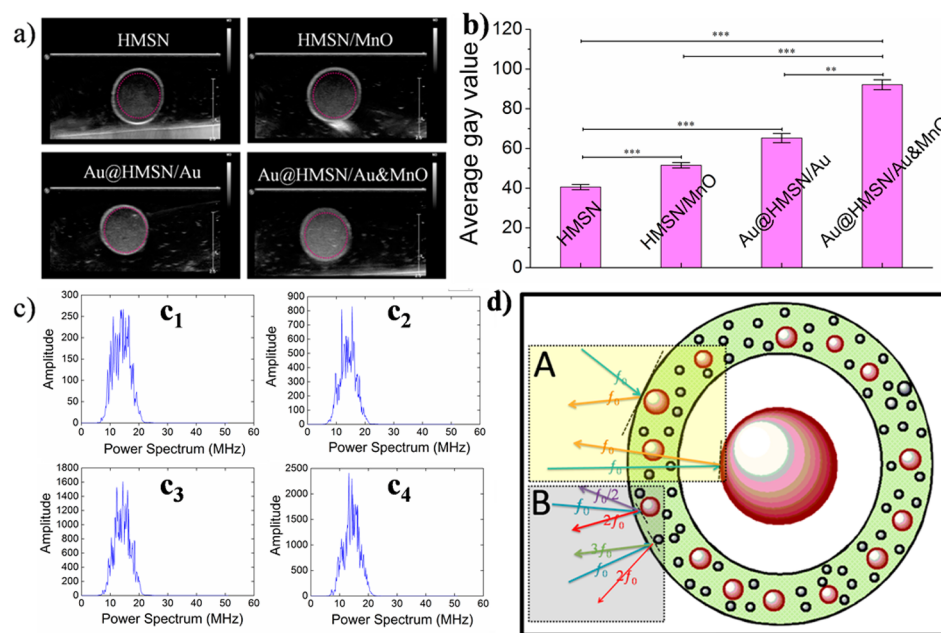

Figure 3. In vitro US imaging evaluations of Au@HMSN/Au&MnO nanoparticles. (a) Acquired ultrasonic images using HMSN, HMSN/MnO, Au@HMSN/Au, and Au@HMSN/Au&MnO nanoparticles as UCAs under BFI. Mechanical index (MI) is 0.6, the gain is kept at 10 dB, and the particle concentration is 3.18×10^8/mL (10 mg/mL). (b) Average gray value obtained from corresponding zone of interest circled by dotted pink circle in a, ** and *** represent P values less than 0.005 and 0.001, respectively. (c) Scattering frequency spectral of (c_1) HMSN, (c_2) HMSN/ MnO, (c_3) Au@HMSN/Au, and (c_4) Au@HMSN/Au&MnO. (d) Schematic image on principle of double-scattering and enhanced nonlinear scattering in a single Au@HMSN/Au&MnO nanoparticle in intensifying MR imaging, and noting: A zone represents double-backscattering that occurs at outer surfaces of the whole probe particle and the larger Au nanoparticle, respectively, and B zone presents enhanced nonlinear scattering by the smaller Au nanocrystals and MnO nanoparticles that induces ultraharmonics ($2f_0$, $3f_0$, ...) and subharmonics ($f_0/2$).

ultimately constructing a heterogeneous rattle-type Au@ HMSN/Au&MnO nanoparticles (Figure 1a−h).

Reducing ability of amino groups has been elaborately validated in our previous work,[20,21] which are demonstrated in Figure 1 and Figure S1b1−b3. Despite depletion of some amino groups when preparing Au@HMSN/Au, residual amino

groups can remain as reducing agent to further manufacture noncrystalline MnO nanoparticles (Figures 1a−h and 2c,e,f). Employing this *in situ* self-reduction approach could make Mn paramagentic centers uniform.[22] Noticeably, after amino-mediated SSR process, all of the values of pore size (Figures 2b and Fgure S2), BET surface area and pore volume (Table
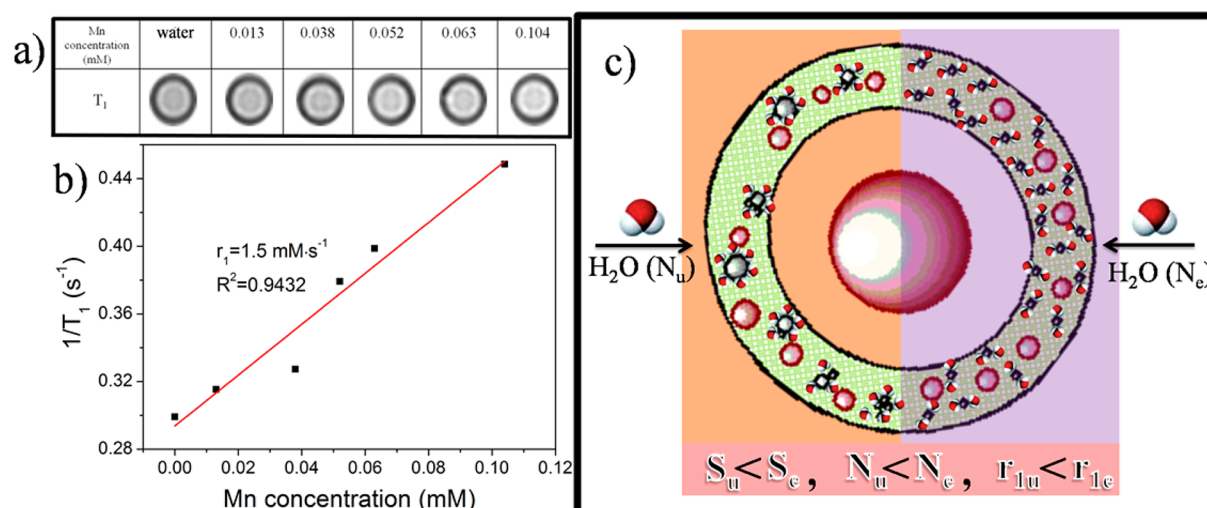
Figure 4. In vitro evaluations of Au@HMSN/Au&MnO as CAs in intensifying MR imaging. (a) In vitro T_1-weighted MRI images; (b) T_1 relaxivity plot of aqueous solutions of Au@HMSN/Au&MnO at different concentrations. (c) Schematic image on principle comparison in intensifying MR imaging between uniformly distributed MnO nanoparticles (right) and MnO aggregates (left), and noting that S_u and S_e represent the surface area per unit mass of MnO aggregates and uniformly distributed MnO nanoparticles, respectively; N_u and N_e represent the number of H_2O molecules coordinated with MnO aggregates and uniformly distributed MnO nanoparticles, respectively; r_{1u} and r_{1e} represent the longitudinal relaxivity of MnO aggregates and uniformly distributed MnO nanoparticles, respectively.

S1) increase, which can be attributed to the simultaneous erosion of SiO_2 framework by strong oxidant, $KMnO_4$ when reacting with oxided aminopropyl chains. Nevertheless, the particle diameter (Figure 1a−h and Figure S3) of Au@HMSN/Au&MnO and the size (Figures 1a−h and 2d and Figure S1b1−b3) and crystallinity (Figure 2e) of loaded Au nanoparticles remain unchanged after reaction with $KMnO_4$. Additionally, absence of Au NPs or NCs (Figure S1c1-c3) due to the complete exhaustion of amino groups by $KMnO_4$ (Figure S4) when amino groups-functionalized HMSNs first reacted with $KMnO_4$ and subsequently with $HAuCl_4$ indicates the amino groups-mediated SSR process is irreversible. According to ICP analysis, the percentages of Mn and Au in Au@HMSN/Au&MnO nanoparticles are 25 and 5%, respectively.

Structural Superiority of Au@HMSN/Au&MnO in Intensifying US Imaging. Despite substantial advances in understanding and exploring how to improve imaging performance of inorganic component-based UCAs,[23] the inherent drawback, poor elasticity, remains a problematic concern. Comparing to the composition design theory, structure optimization design is an ideal route, which is desired for inorganic UCAs. Very recently, a facilely available structure design concept on UCAs, double scattering/reflection in a single nanoparticle for intensifying US imaging, has been proposed and experimentally and theoretically validated.[24] Moreover, another available structure design concept that is adding some nanoparticles in shell of UCAs to improve ultrasound imaging via promoting nonlinear scattering has been also experimentally accepted.[25−27]

Inspired by this, we incorporated the principles of above two structure design concepts, and further integrate them into design of US&CT&MR trimodal imaging probe, and the special structure of as-prepared Au@HMSN/Au&MnO indeed perfectly caters to above-mentioned two structure design concepts. As shown in Figure 3d, the large Au nanoparticle in the hollow cavity of HMSNs can expectedly provide the second interface to promote occurrence of double scattering/

reflection together with outer surface of integral particle (A zone), whereas some lots of smaller Au nanocrystals and MnO nanoparticles are expected to enhance nonlinear scattering (B zone), i.e., promoting emergence of ultraharmonics ($2f_0$, $3f_0$, etc.) and subharmonics ($f_0/2$), both of which will expectedly improve US imaging ability of this trimodal imaging probe.[25,26] To validate the superiority of combination between double-backscattering and enhanced nonlinear scattering in intensifying US imaging, we chose three other types of nanoparticles of the same particle diameter with Au@HMSN/Au&MnO (Figure S3) as comparisons, i.e., HMSNs, Au@HMSN/Au and HMSN/MnO (Figure S1c). It can be clearly observed (Figure 3a, b) that HMSN/MnO nanoparticles acquire more excellent imaging ability than HMSNs, suggesting that MnO nanoparticle in shell helped HMSNs to scatter more US waves. A larger increment of gray value using Au@HMSN/Au than using HMSN/MnO relative to HMSNs can be attributed to the emergence of double scattering in a single Au@HMSN/Au nanoparticle. When combining the two aspects, a synergistic effect can be obtained, because a much larger increment (46.9) from HMSN to Au@HMSN/Au&MnO than sum of that (9.9) from HMSN to HMSN/MnO and that (22.5) from HMSN to Au@HMSN/Au is found. The results convincingly validate the reasonability of combination of above-mentioned two structure design concepts. Scattering measurements (Figure 3c) wherein the amplitude progressively increase from HMSN, to HMSN/MnO, to Au@HMSN/Au, and ultimately to Au@HMSN/Au&MnO also demonstrates the coexistence of strong double-scattering and nonlinear scattering via comparison and analysis when using Au@HMSN/Au&MnO as UCAs. Additionally, it can be calculated that the contribution of double-scattering is 48%, and the contribution of nonlinear scattering is 52% (see details in the Experimental Section).

Apart from excellent imaging ability, structure stability is another pivotal concern for UCAs. Despite enhancing nonlinear scattering to improve US imaging, adding metal or oxide nanoparticles with higher density than matrix in shell could also substantially enhance the structure stability of UCAs.[25,26] In
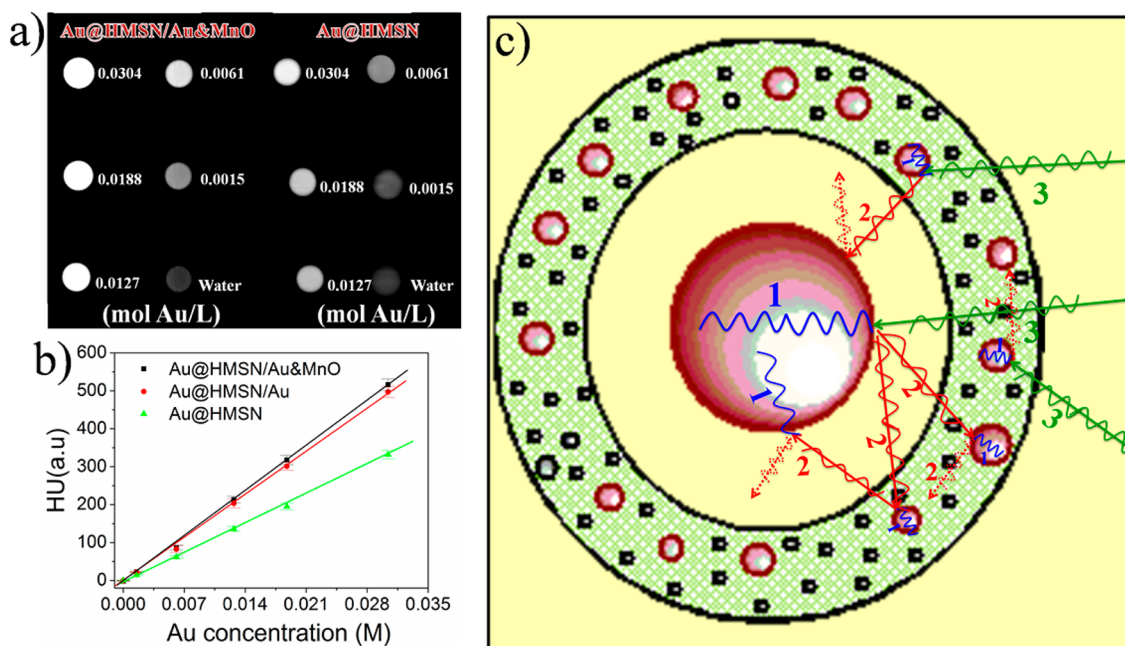
Figure 5. In vitro evaluations of Au@HMSN/Au&MnO as CAs in intensifying CT imaging. (a, b) In vitro CT images (a) and CT value (HU) plots of aqueous solutions of Au@HMSN/Au&MnO and Au@HMSN at different concentrations, and Au@HMSN/Au performs similar to Au@HMSN/Au&MnO, indicating MnO plays a neglectable role in enhancing CT imaging; notes: the slopes of the concentration-dependent profile of HU are 17333 M^{-1} for Au@HMSN/Au&MnO, 16500 M^{-1} for Au@HMSN/Au and 11035 M^{-1} for Au@HMSN. (c) Schematic image on principle of "core−satellite" structure of Au in intensifying CT imaging, and noting: blue 1 represents absorption of X-ray, red 2 represents scattering of X-ray, and green 3 represents incident X-ray, wherein absorption (blue 1) is responsible for CT imaging.

Figure S5, the contrast using the trimodal probe as UCAs accordingly increases as the mechanical index increases. Additionally, with the increase of mass concentration, US imaging performance also gradually increases, as shown in Figure S6. It is noteworthy that Au@HMSN/Au&MnO nanoparticles also share the much longer duration than conventional organic microbubbles owing its stable structure, as shown in Figure S7.

Structural Superiority of Au@HMSN/Au&MnO in Intensifying MR Imaging. Manganese-based oxides have been validated as alternative CAs for T_1-weighted MRI (T_1-MRI) to potentially replace clinical gadolinium-based CAs because of their excellence in biocompatibility,[28−30] as gadolinium can instigate nephrogenic systemic fibrosis. However, the imaging ability of Mn-based nanoparticles (typically $r_1 < 0.5$ mM^{-1} s^{-1}) was considerably inferior to those of commercial gadolinium-based CAs ($r_1 \approx 3.4$ mM^{-1} s^{-1}).[31]

Very recently, a method of uniformly distributing MnO nanoparticles via in situ reaction between templates ($C_{16}TAB$) in MSN and $KMnO_4$ has been established,[22] which is beneficial for improving T_1-weighted MR imaging. Given this, the remaining amino groups after reducing Au precursor that are clearly shown in Figure 2c (N−H vibration peak in Au@HMSN/Au) and Figure S8 (positively charged Au@HMSN/Au) can act like $C_{16}TAB$ to reduce $KMnO_4$ to in situ generate uniformly distributed Mn_xO nanoparticles. After further thermal reduction under reducing gas atmosphere, the as-prepared MnO nanoparticles uniformly distribute in mico- or meso- channels that can confine overgrowth of MnO nanoparticles (Figure 1h), and Figure S9 demonstrates the as-prepared Au@HMSN/Au&MnO nanoparticles are indeed paramagnetic. Figure 4c shows why uniform distribution Mn paramagentic centers perform much better in improving T_1-

weighted MR imaging than MnO aggregates, wherein it indicates that uniformly distributed MnO nanoparticles share a larger surface area, thus can allow more coordinated water molecules,[17] ultimately resulting in a larger r_1 value in comparison to MnO aggregates. As expected, the highly uniform distribution of Mn paramagnetic centers in shell allows Au@HMSN/Au&MnO to definitely harvest a more excellent T_1-MRI ability ($r_1 = 1.5$ mM^{-1} s^{-1}) than the common MnO nanoparticles (typically $r_1 = 0.61$ mM^{-1} s^{-1}), as shown in Figure 4a, b and Figure S10. Additionally, because MnO-based nanoparticles could act as T_2-weighted MR contrast agents,[32] herein, the Au@HMSN/Au&MnO displays an excellent T_2-MRI ability ($r_2 = 53$ mM^{-1} s^{-1}), as shown in Figure S11.

Structural Superiority of Au@HMSN/Au&MnO in Intensifying CT Imaging. The clinically used CT contrast agents, iodinated compounds, usually suffered from short imaging time and even potential renal toxicity due to their rapid kidney's clearance.[33] Several new CT contrast agents, such as Bi_2S_3, TaO_x and Au NPs were explored to address the shortcomings of iodine agents.[34−36] In comparison to traditional iodinated compounds, Au NPs can be regarded as alternative CAs due to lower toxicity, longer imaging time and higher absorption coefficient over iodine (e.g., at 100 keV, gold, 5.16 cm^2 g^{-1}; iodine, 1.94 cm^2 g^{-1}).[36] However, in previous reports with employing Au as CT CAs, the structure design was rarely taken into consideration.[18,36]

Herein, "core−satellite" structure consisting of the inner large Au nanoparticle and some other smaller Au nanocrystals in shell can be readily obtained via a facile self-reduction, and the silica as linker between core and satellite can be more easily tuned than conventional DNA linkers.[37] The "core−satellite" structure can not only participate the structure design for enhancing US imaging, but can also benefit CT imaging. To demonstrate it, a comparison sample, Au@HMSN (Figure
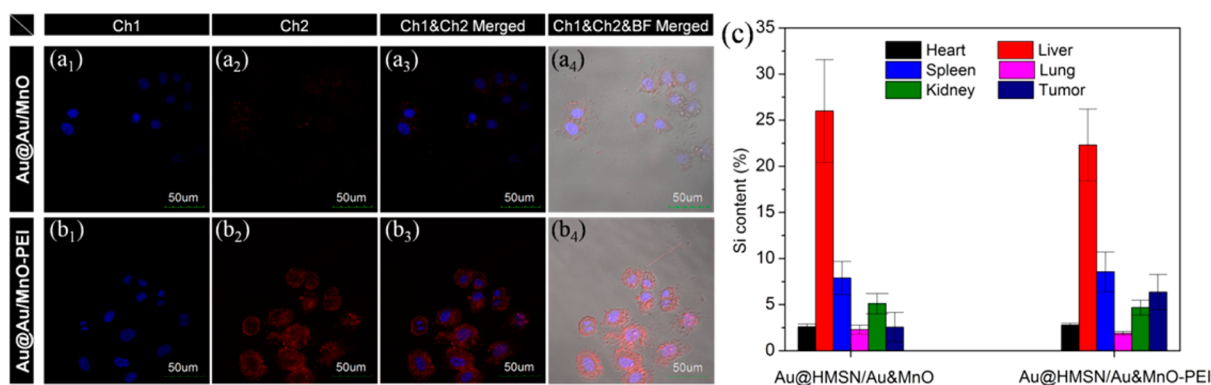
Figure 6. Intracellular and in vivo uptake evaluations of Au@HMSN/Au&MnO with PEI modifications (termed as Au@HMSN/Au&MnO-PEI) by VX2 tumor. (a_1–a_4, b_1–b_4) In vitro confocal images of VX2 cells after incubation with (a_1–a_4) Au@HMSN/Au&MnO and (b_1–b_4) Au@HMSN/Au&MnO-PEI for 2 h; Ch1 channel represents nuclei (blue color) stained by DAPI (Ex = 356 nm)and Ch2 channel represents nanoparticles loading rhodamine 6G (R6G, red color, Ex = 525 nm). (c) In vivo Si content distributions in different organs (heart, liver, spleen, lung, kidney, and tumor) of New Zealand White rabbits bearing VX2 tumor after injecting above two types of nanoparticles for 12 h.
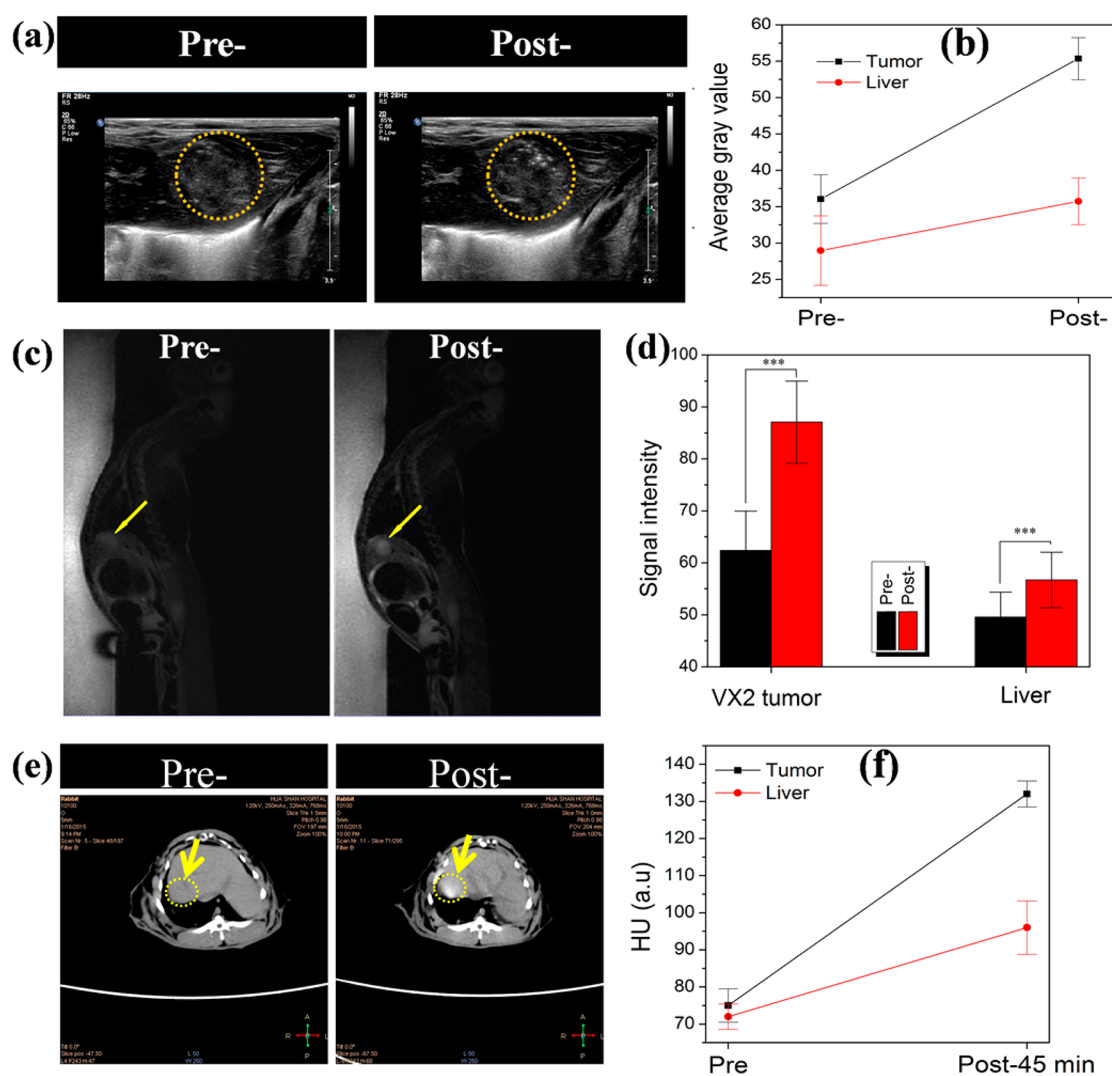

Figure 7. In vivo evaluations of US, CT, and MR trimodal imaging for New Zealand white rabbit bearing VX2 tumor using Au@HMSN/Au&MnO-PEI as CAs. (a) Ultrasonic images using Au@HMSN/Au&MnO-PEI as UCAs under B fundamental imaging (BFI). (b) Corresponding average gray value obtained from corresponding zone of interest circled by dotted pink circle in a. Mechanical index is 0.6, and the injection volume is 3 mL with a particle concentration is 8.48×10^8/mL. (c) T_1-weighted MR contrast images: preinjection (left), postinjection (right), and yellow arrow indicating VX 2 tumor (dose: 3 mg Mn/kg); and (d) T_1 single intensities at tumor site and normal liver: preinjection (dark block) and post injection (red block). (e) CT contrast images: preinjection (left), postinjection (right), and yellow arrow and zone circled by yellow dotted ellipse indicating VX 2 tumor (dose: 19.2 mg Au/kg); and (f) HU value variation at tumor before and after injecting this trimodal imaging probe.

S12b, c) was prepared via a postetching method wherein Au nanoparticles were first synthesized (Figure S12a) and then were encapsulated by dense silica layer and hybrid silica layer, and ultimately the middle dense silica layer was etched out. The selected area electron diffraction pattern (Figure S12d) shows the Au nanoparticles in Au@HMSN are single crystal structure, indicating no Au nanocrystals in shells, or else, diffraction ring characteristic of polycrystalline would emerge instead. Therefore, the structure of Au@HMSN is merely heterogeneous rattle-type rather than "core−satellite" type.

In Figure 5a,b, it shows that the core−satellite (either Au@ HMSN/Au&MnO or Au@HMSN/Au) acquired brighter contrast and larger HU value than Au@HMSN under the same Au molar concentration, and performed better than that in previous reports.[18] This phenomenon can be probably attributed to more X-ray absorption by this special "core−satellite" structure than common Au nanoparticles, as shown in Figure 5c, wherein besides the first absorption, the second absorption after first scattering or the third absorption after the second scattering probably remain existing, and multiple absorptions can substantially improve utilization efficiency of X-ray, and then promote CT imaging. The unique advantage of such a "core−satellite" structure in enhancing CT imaging can be further demonstrated via comparing to Au nanoparticles modified with PEG molecules (Figure S13).

In Vivo Evaluations of Au@HMSN/Au&MnO as Trimodal CAs in Intensifying US, MR, and CT Imaging. To maximally improve the trimodal imaging performance of such a trimodal imaging probe, maximum accumulation in tumor is indispensible. In previous report, it has been validated that positively charged nanoparticles can be more accessible to uptake by tumor cells.[38] Herein, we employed positively charged polyethylenimine (PEI, MW = 1800) that was usually regarded as nonviral gene vectors,[39] as modified agent to modify Au@HMSN/Au&MnO nanoparticles via electrostatic adsorption force. After PEI modifications, zeta potential increases from −19.8 mV to 43.3 mV (Figure S8), and the particle hydrated diameter also increases from 431 to 489 nm. As expected, after PEI modification, much more probes represented by red color (R6G) are engulfed by VX2 rabbit tumor cells (Figure 6a$_1$–a$_4$ and 6b$_1$–b$_4$). Furthermore, in vivo accumulation of Au@HMSN/Au&MnO-PEI (6.39%) in VX2 tumor is more than 2-fold higher than that of Au@HMSN/ Au&MnO (2.52%) (Figure 6c). Importantly, no evident in vitro cytotoxicity and in vivo tissue toxicity after 30 days can be found in Figures S14 and S15, respectively, suggesting Au@ HMSN/Au&MnO-PEI possesses an excellent biocompability.

Figure 7a, b shows in vivo US imaging outcomes using the PEI-modified trimodal imaging probe (Au@HMSN/ Au&MnO-PEI nanoparticles) as UCAs. Thanks to the substantially enhanced accumulation in tumor mediated by positively charged modification, a larger contrast increment can be clearly found after injecting Au@HMSN/Au&MnO-PEI for 1 h under B fundamental imaging (BFI) mode than that in normal liver, confirming that this trimodal imaging probe can intensify in vivo US imaging for tumor.

This trimodal imaging probes also can be regarded as MR CAs to promote the capability of MR imaging. In in vitro evaluation, relying on the highly uniform distribution of Mn paramagentic centers, T_1-weighted MR imaging can be greatly enhanced and the r_1 value is 3 times larger than that in previous report.[29] Together with contribution from positively charged PEI modification, MR signal intensity in VX2 tumor implanted

in liver of New Zealand white rabbit increases from 63 to 87 after administering this nanoprobe (Figure 7c,d), evidently higher than the incremental value of MR single intensity in normal liver. Similarly, thanks to the contributions from positively charged PEI modification and the special "core−satellite" structure, this trimodal probing probes can act as excellent CT CAs to enhance contrast of CT slice of VX 2 tumor (Figure 7e, f), wherein HU value increases from 75 to 130 after injecting this trimodal imaging probe in tumor and the increment is much larger than that in normal liver.

■ CONCLUSIONS

In summary, a rational marriage design concept of structure and composition has been proposed, overcoming the common simple-assembly of active building blocks in previous reports, e.g., complex processes and discounted functions of each active component. To exemplify this marriage design strategy, a novel trimodal imaging probe combining US, MR and CT has been obtained using the well-established SSR synthetic approach. In design of such a trimodal imaging probe, a large Au nanoparticle located in the trimodal imaging probe and some smaller Au nanocrystals & MnO nanoparticles embedded in shell promoted the occurrence of double-scattering and enhanced nonlinear scattering, respectively, collaboratively improving US imaging outcomes in vitro. Additionally, highly uniform distribution of Mn paramagentic centers and "core−satellite" structure consisting of some small Au nanocrystals and a large Au nanoparticle have been validated to favor T_1-MRI outcomes and CT imaging in vitro. In this context, such a novel trimodal imaging probe evidently intensified in vivo US, MR, and CT imaging, highlighting a greatly potential future in early diagnosis. More importantly, this design strategy and the involved principles in constructing such a US&MR&CT trimodal imaging probe promise great potentials in guiding designs of other materials-based multimodal imaging probe, and pave a new avenue to optimizing and improving imaging ability of each building block.

■ EXPERIMENTAL SECTION

Materials. Tetraethoxysilane (TEOS, A.R), ammonia solution ($NH_3 \cdot H_2O$) (25−28%, A.R) and sodium carbonate anhydrous (Na_2CO_3, A.R) were obtained from Shanghai Lingfeng Chemical Reagent Co.Ltd. Ethyl alcohol absolute (EtOH) was obtained from Shanghai Zhenxing No.1 Chemical Plant. 3-Aminopropyltriethoxysilane (98%) was purchased from J&K Scientific Ltd. Chloroauric acid ($HAuCl_4 \cdot 4H_2O$, A.R) was obtained from Shanghai Fine Chemical Materials Research Institute. Rhodamine 6G (R6G, 90%) was purchased from ACROS ORGANICS. PEG-SH, manganese(II) acetylacetonate (MnACAC), benzyl ether, oleic acid, potassium permanganate and Poly(ether imide) (MW = 1800) were purchased from sigma-aldrich. Deionized water and ethanol were used in all experiments.

Au@HMSN/Au&MnO, HMSN/Mn$_x$O, and HMSN/MnO Synthesis. 400 mg of amino group functionalized HMSNs were uniformly dispersed into 15 mL of $HAuCl_4$ solution (0.05 M) by sonication, followed by a simple hydrothermal treatment for 2 h under 80 °C, obtaining the heterogeneous rattle-type nanostructure, Au@HMSN/ Au nanoparticles. The immediate product, Au@HMSN/Au nanoparticles were collected via centrifugation, and then were immediately redispersed into 10 mL of aqueous $KMnO_4$ solution (0.4 M) and reacted for 6 h under room temperature, yielding Au@HMSN/ Au&Mn$_x$O. Finally, the trimodal imaging probe was washed for several times until the supernatant was transparent, and then was dried under vacuum. The dried sample was placed into the crucible and calcined for 10 h under reducing atmosphere (5% H_2—95%Ar) at 400 °C,

yielding Au@HMSN/Au&MnO. When directly using amino group functionalized HMSNs to react with $KMnO_4$ solution, $HMSN/Mn_xO$ was first yielded, followed by generating HMSN/MnO via reduction by 5% H_2-95% Ar at 400 °C.

Preparations of Au@HMSN and PEG-Coated Au. *Au@HMSN.* APTES solution in EtOH was added into $HAuCl_4$ solution (0.05 M) in EtOH, followed by a simple hydrothermal treatment for 2 h under 80 °C, obtaining Au nanoparticles. Au nanoparticles were dispersed in a mixture containing 71.6 mL of EtOH, 10 mL of deionized water, and 3.14 mL of ammonia solution, and then 4.28 mL of TEOS was added into the above mixture and reacted for 40 min, obtaining Au nanoparticles encapsulated by a layer of dense silica, afterward another mixture including 2 mL of APTES and 5 mL of TEOS was added and reacted for another 80 min. Ultimately, silica-encapsulated Au nanoparticles were redispersed into 20 mL of aqueous Na_2CO_3 (0.6 M) and treated at 80 °C for 40 min to etch out the middle dense silica layer, obtaining Au@HMSN.

PEG-Coated Au Nanoparticles. above obtained Au nanoparticles in 10 mL aqueous solution were mixed with PEG-SH (1 mg) and stirred for 1 h to covalently modify the surface of the Au nanoparticles with PEG. The resulting PEG-coated Au nanoparticles were collected by centrifugation at 16,000g for 30 min and washed twice with distilled water.

HMSNs Platform Synthesis. In a typical process: 71.6 mLof EtOH, 10 mL of deionized water, and 3.14 mL of ammonia solution were mixed in a wide-mouth bottle and stirred for 30 min, 6 mL of TEOS was added into the above mixture and hydrolyzed, nucleated, and grown for 40 min under magnetic stirring to generate solid silica core, and afterward another mixture consisting of 2 mL of APTES and 5 mL TEOS was dropwise added and stirred for another 80 min. Finally, the product was washed with deionized water centrifuged and redispersed into 50 mL of aqueous Na_2CO_3 (0.6 M) and treated under 80 °C for 60 min to obtain amino groups functionalized HMSNs, and the ultimate product is centrifuged and washed for three times.

Preparation of MnO Nanoparticles. Two millimoles of MnACAC was dissolved in 20 mL of benzyl ether, and then 2 mL of oleic acid was added. While stirring, the solution was then rapidly heated to 280 °C under nitrogen gas for 3 h, after which it was cooled to room temperature. The MnO nanoparticles were washed and precipitated by ethanol, collected by centrifugation at 12 000 rpm for 10 min.

Loading of R6G by Au@HMSN/Au&MnO. One hundred milligrams of Au@HMSN/Au&MnO nanoparticles were dispersed into 20 mL of R6G solution in DMSO and then stirred for 24 h. Afterward, the R6G-loaded Au@HMSN/Au&MnO nanoparticles were collected via centrifugation, and washed 1 time with DMSO and 2 times with deionized water. The ultimate sample was then dried under vacuum.

Calculation on Contributions of Nonlinear Scattering and Double-Scattering in Au@HMSN/Au&MnO for Ultrasound Imaging. Herein, a represents the incremental value that MnO-induced nonlinear scattering causes; b represents the incremental value that small Au nanoparticles-induced nonlinear scattering causes; c represents the incremental value that the large Au nanoparticle-induced double-scattering causes. Because the majority of MnO nanoparticles is much more than that of small Au nanoparticles (Figure 1g, h), $b \ll a$. Noticeably, the increment value (9.9) from HMSN to HMSN/MnO is smaller than that (22.5) from HMSN to Au@HMSN/Au, which means $a < c + b$. Furthermore, it is obtained that the contribution of nonlinear scattering caused by several small Au nanoparticles embedded in Au@HMSN/Au is much smaller than that the contribution of double-scattering caused by the large Au nanoparticle centering at the cavity of Au@HMSN/Au. Therefore, the incremental value that the large Au nanoparticle-induced double-scattering causes is 22.5. Because the size of the large Au nanoparticle in the cavity of Au@HMSN/Au&MnO is identical to that in the cavity of Au@HMSN/Au, the contribution value caused by the large Au nanoparticle-induced double-scatteringremains 22.5, the contribution percentage of double-scattering in Au@HMSN/Au&MnO is 22.5/46.9×100% = 48%, whereas the contribution percentage of nonlinear

scattering that small Au nanoparticles and MnO nanoparticles induce is 52%.

Modification of Au@HMSN/Au&MnO with PEI_{1800} (Au@HMSN/Au_{1800}). Typically, 10 mg of Au@HMSN/Au&MnO or R6G/Au@HMSN/Au&MnO nanoparticles was dispersed into 20 mL of aqueous PEI solution (MW = 1800, 10 wt %) and stirred for 12 h, and then were centrifuged and washed with water for several times. Finally, the product was dried under vacuum for 12 h.

Cell Viability and Proliferation Assay. Fibroblast cells L929 were cultured at 37 °C under 5% CO_2 in Roswell Park Memorial Institute medium (RPMI) 1640 supplemented with 10% FBS and 1% penicillin/streptomycin. Both cells were purchased from Shanghai Institutes for Biological Sciences, China. In vitro cytotoxicity and cell proliferation were assessed using the typical 3-(4,5-dimethylthiazol-2-yl)-2,5-diphenyltetrazolium bromide (MTT) assay. Cells seeded in a 96-well cell-culture plate at a density of 1×10^4 cells per well were cultured in 5% CO_2 at 37 °C for 24 h. Then the medium was replaced with fresh medium containing Au@HMSN/Au&MnO-PEI_{1800} nanoparticles with varied concentrations, and further incubated for 24 or 48 h. Finally, the cell viability was assessed using the MTT assay.

Luminescence Imaging. Confocal luminescence imaging was performed with an Olympus FV1000 laser scanning confocal microscope and a 60 × oil-immersion objective lens. The VX2 cells, seeded in two 35 mm glass-bottomed culture dishes, were washed with PBS buffer and then incubated with R6G/Au@HMSN/Au&MnO-PEI_{1800} and R6G/Au@HMSN/Au&MnO nanoparticles with the same particle concentration for 2 h at 37 °C, respectively. After being washed three times with PBS, the cells were then stained with DAPI solution for 15 min, another three times wash was conducted to remove the reluctant DAPI solution, and after that 500 μL buffer A solution was added to examine endocytosis of Au@HMSN/Au&MnO-PEI_{1800} nanoparticles by VX 2 cells on confocal luminescence imaging.

In Vitro and in Vivo US Imaging Using Au@HMSN/Au&MnO-PEI_{1800} As US Imaging CAs. The as-synthesized Au@HMSN/Au&MnO-PEI of a certain concentration was placed and sealed in an elastic rubber bag, and then the bag was immersed into a cistern full of PBS solution. The detector of ultrasound imaging instrument was fixed on the position with spacing of 2.8 cm from the elastic rubber bag filled with undetermined sample solution (the particle concentration is 3.18×10^8/ml (10 mg/mL)), especially 2.8 cm spacing is the most optimal value. The received signals were converted into images exhibited on the screen. The average gray values can be obtained from an image processing software, Somomath—Dicom. In all in vitro experiments, the broadband excitation frequency centering at 10 MHz with a bandwidth of 8−12 MHz was employed, The parameters of Philips IU 22 are as follows: the transducer is L12−5, the mechanical index (MI) is 0.6, the gain is kept at 10 dB, and other setting parameters are that software: QLAB, mode: SmPrt Sup, frame frequency (FR): 32 Hz.

New Zealand white rabbits, weighing 2.5−3.0 kg were supplied by laboratory Animal Center of Shanghai Tenth Peoples' Hospital. All animal experiments in this study were performed according to protocols approved by the Laboratory Animal Center of Shanghai Tenth Peoples' Hospital and were in accordance with the policies of National Ministry of Health. VX2 tumor−bearing rabbits were fasted for 24 h before experiments and their abdomen and back were shaved. After the rabbit was anesthetized and fixed, 3 mL of Au@HMSN/Au&MnO-PEI_{1800} solution with a particle concentration is 8.48×10^8/ml dispersed in PBS was injected into VX2 tumor. Ultrasonic images before and after intravenous injection of Au@HMSN/Au&MnO-PEI_{1800} dispersion were recorded under B fundamental imaging mode, tissue harmonic imaging mode and contrast harmonic imaging mode. Under THI mode, the mechanical index (MI) is 0.7 and the frame frequency (FR) is 15 Hz; under BFI mode, the mechanical index (MI) is 0.6 and frame frequency (FR) is 28 Hz; under CHI mode, the mechanical index (MI) is 0.07 and frame frequency (FR) is 9 Hz.

In Vitro and in Vivo MR Imaging Using Au@HMSN/Au&MnO-PEI1800 As MR Imaging CAs. The T_1-weighted MR imaging in vitro was performed on a 3.0 T clinical MRI instrument

(GE Signa 3.0 T), and the pulse sequence used was a T_1-weighted FSE-XL/90 sequence. Aqueous dilutions of Au@HMSN/Au&MnO-PEI$_{1800}$ with varied Mn molar concentrations were placed in a series of 1.0 mL centrifugal tube for T_1-weighted MR imaging and alined sequentially. Mn content in Au@HMSN/Au&MnO-PEI$_{1800}$ was determined by inductively coupled plasma atomic emission spectrometry (ICP-AES). The resulting T_1 values were recorded at different concentration and plotted as $1/T_1$ vs molar concentration of Mn. And then the slope of this line provides the molar relaxivity, r_1 value.

In vivo MR imaging of VX2 tumor were carried out on VX2 tumor-bearing New Zealand white rabbit. CT imaging was conducted before and after 1 h of intravenous administration of Au@HMSN/Au&MnO-PEI$_{1800}$ dispersion (dosage: 3 mg Mn/kg for CT imaging). All animal experiments in this study were performed according to protocols approved by the Laboratory Animal Center of Shanghai Tenth Peoples' Hospital and were in accordance with the policies of National Ministry of Health.

In Vitro and in Vivo Imaging Using Au@HMSN/Au&MnO-PEI1800 As CT Imaging CAs. The CT tests in vitro and in vivo were performed on a 64-section multi detector row computed tomography scanner (GE discovery CT750 HD, GE Healthcare). CT imaging of Au@HMSN/Au&MnO-PEI$_{1800}$ was conducted with water as the reference. Au@HMSN/Au&MnO-PEI$_{1800}$ dispersion was serially diluted in 1.0 mL of water at varied concentrations. Au and Mn contents in Au@HMSN/Au&MnO-PEI$_{1800}$ were determined by inductively coupled plasma atomic emission spectrometry (ICP-AES). CT imaging for samples were finally calculated in Hounsfield units (HU) by averaged over the 3D-based region of interest (ROI).

In vivo MR imaging of VX2 tumor were implemented on VX2 tumor-bearing New Zealand white rabbit. T_1-weighted MR images were recorded, respectively, before and after 1 h of intravenous administration of Au@HMSN/Au&MnO-PEI$_{1800}$ dispersion (dosage: 19.2 mg Au/kg for CT imaging). All animal experiments in this study were performed according to protocols approved by the Laboratory Animal Center of Shanghai Tenth Peoples' Hospital and were in accordance with the policies of National Ministry of Health. After another 30 days, the rabbits were executed, and tumor and other organs (heart, liver, spleen, lung and kidney) of each rabbit were isolated for staining with hematoxylin and eosin (H&E) staining for histopathological analysis by optical microscope.

ASSOCIATED CONTENT

Ⓢ Supporting Information

The Supporting Information is available free of charge on the ACS Publications website at DOI: 10.1021/acsami.5b04999.

Figures S1−S15 (PDF)

AUTHOR INFORMATION

Corresponding Authors
*E-mail: xuhuixiong@126.com.
*E-mail: hrchen@mail.sic.ac.cn.

Author Contributions
K.Z. conceived and designed the experiments. K.Z., P.L., X.B., X.L., and Z.Z. performed the experiments. K.Z. and H.X. analyzed the data. K.Z., H.X. and H.C. cowrote the paper. All authors discussed the results and commented on the manuscript.

Notes
The authors declare no competing financial interest.

ACKNOWLEDGMENTS

ABBREVIATIONS

CT,computed tomography (CT)
MR,magnetic resonance (MR)
US,ultrasound
UCAs,ultrasound contrast agents
HMSNs,hollow mesoporous silica nanoparticles
NPs,nanopartices
CAs,contrast agents
SSR,sequential self-reduction

REFERENCES

(1) Herschman, H. R. Molecular Imaging: Looking at Problems. *Science* **2003**, *302*, 605−608.

(2) Dierolf, M.; Menzel, A.; Thibault, P.; Schneider, P.; Kewish, C. M.; Wepf, R.; Bunk, O.; Pfeiffer, F. Ptychographic X-ray Computed Tomography at the Nanoscale. *Nature* **2010**, *467*, 436−439.

(3) Schröder, L.; Lowery, T. J. Molecular Imaging Using a Targeted Magnetic Resonance Hyperpolarized Biosensor. *Science* **2006**, *314*, 446−449.

(4) Weissleder, R.; Pittet, M. J. Imaging in the Era of Molecular Oncology. *Nature* **2008**, *452*, 580−589.

(5) Wang, L. V.; Hu, S. Photoacoustic Tomography: *In Vivo* Imaging from Organelles to Organs. *Science* **2012**, *335*, 1458−1462.

(6) Narayanan, T. N.; Gupta, B. K.; Vithayathil, S. A.; Aburto, R. R.; Mani, S. A.; Taha-tijerina, J.; Xie, B.; Kaipparettu, B. A.; Torti, S. V.; Ajayan, P. M. Hybrid 2D Nanomaterials as Dual-Mode Contrast Agents in Cellular Imaging. *Adv. Mater.* **2012**, *24*, 2992−2998.

(7) Zhang, K.; Chen, H.; Li, F.; Wang, Q.; Zheng, S.; Xu, H.; Ma, M.; Jia, X.; Chen, Y.; Mou, J.; Wang, X.; Shi, J. A Continuous Tri-phase Transition Effect for HIFU-mediated Intravenous Drug Delivery. *Biomaterials* **2014**, *35*, 5875−5885.

(8) Hak, S.; Helgesen, E.; Hektoen, H. H.; Huuse, E. M.; Jarzyna, P. A.; Mulder, W. J. M.; Haraldseth, O.; Davies, C. D. L. The Effect of Nanoparticle Polyethylene Glycol Surface Density on Ligand- Directed Tumor Targeting Studied in Vivo by Dual Modality Imaging. *ACS Nano* **2012**, *6*, 5648−5658.

(9) Wang, C.; Ma, X.; Ye, S.; Cheng, L.; Yang, K.; Guo, L.; Li, C. Protamine Functionalized Single-Walled Carbon Nanotubes for Stem Cell Labeling and *In Vivo* Raman/Magnetic Resonance/Photoacoustic Triple-Modal Imaging. *Adv. Funct. Mater.* **2012**, *22*, 2363−2375.

(10) Lux, F.; Mignot, A.; Mowat, P.; Louis, C.; Dufort, S.; Bernhard, C.; Denat, F.; Boschetti, F.; Brunet, C.; Antoine, R.; Dugourd, P.; Laurent, S.; et al. Ultrasmall Rigid Particles as Multimodal Probes for Medical Applications. *Angew. Chem., Int. Ed.* **2011**, *50*, 12299−12303.

(11) Liu, Z.; Pu, F.; Huang, S.; Yuan, Q.; Ren, J.; Qu, X. Long-circulating Gd$_2$O$_3$:Yb^{3+},Er^{3+} Up-conversion Nanoprobes as High-performance Contrast Agents for Multi-modality Imaging. *Biomaterials* **2013**, *34*, 1712−1721.

(12) Kim, J. S.; Rieter, W. J.; Taylor, K. M. L.; An, H.; Lin, W.; Lin, W. Self-Assembled Hybrid Nanoparticles for Cancer-Specific Multi-modal Imaging. *J. Am. Chem. Soc.* **2007**, *129*, 8962−8963.

(13) Zhao, H. Y.; Liu, S.; He, J.; Pan, C. C.; Li, H.; Zhou, Z. Y.; Ding, Y.; Huo, D.; Hu, Y. Synthesis and Application of Strawberry-like Fe$_3$O$_4$-Au Nanoparticles as CT-MR Dual-modality Contrast Agents in Accurate Detection of the Progressive Liver Disease. *Biomaterials* **2015**, *51*, 194−207.

(14) Feng, W.; Zhou, X.; Nie, W.; Chen, L.; Qiu, K.; Zhang, Y.; He, C. Au/Polypyrrole@Fe$_3$O$_4$ Nanocomposites for MR/CT Dual-Modal Imaging Guided-Photothermal Therapy: An in Vitro Study. *ACS Appl. Mater. Interfaces* **2015**, *7*, 4354−4367.

(15) Liu, B.; Li, C.; Ma, P.; Chen, Y.; Zhang, Y.; Hou, Z.; Huang, S.; Lin, J. Multifunctional NaYF4:Yb, Er@mSiO$_2$@Fe$_3$O$_4$-PEG Nanoparticles for UCL/MR Bioimaging and Magnetically Targeted Drug Delivery. *Nanoscale* **2015**, *7*, 1839−1848.

(16) Liu, L.; Tang, C.; Zhang, Y.; Zang, C.; Zhang, D.; Xiao, H.; Qin, R.; Bao, Z. Influence of SiO_2 Coating on Morphology, Phase and Upconversion Luminescence Properties of $NaYF_4$:Yb^{3+},Er^{3+} Submicrocubes during Annealing. *J. Alloys Compd.* 2014, *591*, 320−325.

(17) Chen, F.; Bu, W.; Zhang, S.; Liu, J.; Fan, W.; Zhou, L.; Peng, W.; Shi, J. Gd^{3+}-Ion-Doped Upconversion Nanoprobes: Relaxivity Mechanism Probing and Sensitivity Optimization. *Adv. Funct. Mater.* 2013, *23*, 298−307.

(18) Wang, L.; Xing, H.; Zhang, S.; Ren, G.; Pan, L.; Zhang, K.; Bu, W.; Zheng, X.; Zhou, L.; Peng, W.; Hua, Y.; Shi, J. A Gd-doped Mg-Al-LDH/Au Nanocomposite for CT/MR Bimodal Imagings and Simultaneous Drug Delivery. *Biomaterials* 2013, *34*, 3390−3401.

(19) Wen, S.; Wen, S.; Li, K.; Cai, H.; Chen, Q.; Shen, M.; Huang, Y.; Peng, C.; Hou, W.; Zhu, M.; Zhang, G.; Shi, X. Multifunctional Dendrimer-entrapped Gold Nanoparticles for Dual mode CT/MR Imaging Applications. *Biomaterials* 2013, *34*, 1570−1580.

(20) Zhang, K.; Chen, H.; Zheng, Y.; Chen, Y.; Ma, M.; Wang, X.; Wang, L.; Zeng, D.; Shi, J. A Facile In-situ Hydrophobic Layer-protected Selective Etching Strategy for the Synchronous Synthesis/Modification of Hollow or Rattle-type Silica Nanoconstructs. *J. Mater. Chem.* 2012, *22*, 12553−12561.

(21) Zhang, K.; Chen, H.; Zhou, X.; Gong, Y.; Zhang, G.; Wang, X.; Chen, Y.; Shi, J. Unconventional Pd Nanoparticles' Growth Induced by a Competitive Effect between Temperature-dependent Coordination and Reduction of Grafted Amino Ligands for Heck Reaction. *J. Mater. Chem. A* 2014, *2*, 1515−1523.

(22) Dong, X.; Shen, W.; Zhu, Y.; Xiong, L.; Shi, J. Facile Synthesis of Manganese-Loaded Mesoporous Silica Materials by Direct Reaction Between $KMnO_4$ and an In-Situ Surfactant Template. *Adv. Funct. Mater.* 2005, *15*, 955−960.

(23) Lin, P. L.; Eckersley, R. J.; Hall, E. A. H. Ultrabubble: A Laminated Ultrasound Contrast Agent with Narrow Size Range. *Adv. Mater.* 2009, *21*, 3949−3952.

(24) Zhang, K.; Chen, H.; Guo, X.; Zhang, D.; Zheng, Y.; Zheng, H.; Shi, J. Double-scattering/reflection in a Single Nanoparticle for Intensified Ultrasound Imaging. *Sci. Rep.* 2015, *5*, 8766.

(25) Stride, E.; Pancholi, K.; Edirisinghe, M. J.; Samarasinghe, S. Increasing the Nonlinear Character of Microbubble Oscillations at Low Acoustic Pressures. *J. R. Soc., Interface* 2008, *5*, 807−811.

(26) Cai, X.; Yang, F.; Gu, N. Applications of Magnetic Microbubbles for Theranostics. *Theranostics* 2012, *2*, 103−112.

(27) Malvindi, M. A.; Greco, A.; Conversano, F.; Figuerola, A.; Corti, M.; Bonora, M.; Lascialfari, A.; Doumari, H. A.; Moscardini, M.; Cingolani, R.; Gigli, G.; Casciaro, S.; Pellegrino, T.; Ragusa, A. Magnetic/Silica Nanocomposites as Dual-Mode Contrast Agents for Combined Magnetic Resonance Imaging and Ultrasonography. *Adv. Funct. Mater.* 2011, *21*, 2548−2555.

(28) Kim, T.; Cho, E. J.; Chae, Y.; Kim, M.; Oh, A.; Jin, J.; Lee, E. S.; Baik, H.; Haam, S.; Suh, J. S.; Huh, Y. M.; Lee, K. Urchin-Shaped Manganese Oxide Nanoparticles as pH-Responsive Activatable T-1 Contrast Agents for Magnetic Resonance Imaging. *Angew. Chem., Int. Ed.* 2011, *50*, 10589−10593.

(29) Bennewitz, M. F.; Lobo, T. L.; Nkansah, M. K.; Ulas, G.; Brudvig, G. W.; Shapiro, E. M. Biocompatible and pH-Sensitive PLGA Encapsulated MnO Nanocrystals for Molecular and Cellular MRI. *ACS Nano* 2011, *5*, 3438−3446.

(30) Perez-Rodriguez, J.; Lai, S.; Ehst, B. D.; Fine, D. M.; Bluemke, D. A. Nephrogenic Systemic Fibrosis: Incidence, Associations, and Effect of Risk Factor Assessment-Report of 33 Cases. *Radiology* 2009, *250*, 371−377.

(31) Kim, T.; Momin, E.; Choi, J.; Yuan, K.; Zaidi, H.; Kim, J.; Park, M.; Lee, N.; McMahon, M. T.; Quinones-hinojosa, A.; Bulte, J. W. M.; Hyeon, T.; Gilad, A. A. Mesoporous Silica-Coated Hollow Manganese Oxide Nanoparticles as Positive T-1 Contrast Agents for Labeling and MRI Tracking of Adipose-Derived Mesenchyrnal Stem Cells. *J. Am. Chem. Soc.* 2011, *133*, 2955−2961.

(32) Niu, D.; Luo, X.; Li, Y.; Liu, X.; Wang, X.; Shi, J. Manganese-Loaded Dual-Mesoporous Silica Spheres for Efficient T1-and T2-Weighted Dual Mode Magnetic Resonance Imaging. *ACS Appl. Mater. Interfaces* 2013, *5*, 9942−9948.

(33) Haller, C.; Hizoh, I. The Cytotoxicity of Iodinated Radiocontrast Agents on Renal Cells In Vitro. *Invest. Radiol.* 2004, *39*, 149−154.

(34) Rabin, O.; Perez, J. M.; Grimm, J.; Wojtkiewicz, G.; Weissleder, R. An X-ray Computed Tomography Imaging Agent Based on Long-circulating Bismuth Sulphide Nanoparticles. *Nat. Mater.* 2006, *5*, 118−122.

(35) Oh, M. H.; Lee, N.; Kim, H.; Park, S. P.; Piao, Y.; Lee, J.; Jun, S. W.; Moon, W. K.; Choi, S. H.; Hyeon, T. Large-scale Synthesis of Bioinert Tantalum Oxide Nanoparticles for X-ray Computed Tomography Imaging and Bimodal Image-guided Sentinel Lymph Node Mapping. *J. Am. Chem. Soc.* 2011, *133*, 5508−5515.

(36) Xing, H.; Bu, W.; Zhang, S.; Zheng, X.; Li, M.; Chen, F.; He, Q.; Zhou, L.; Peng, W.; Hua, Y.; Shi, J. Multifunctional Nanoprobes for Upconversion Fluorescence, MR and CT Trimodal Imaging. *Biomaterials* 2011, *33*, 1079−1089.

(37) Schreiber, R.; Do, J.; Roller, E.-M.; Zhang, T.; Schuller, V. J.; Nickels, P. C.; Feldmann, J.; Liedl, T. Hierarchical Assembly of Metal Nanoparticles, Quantum Dots and Organic Dyes Using DNA Origami Scaffolds. *Nat. Nanotechnol.* 2013, *9*, 74−78.

(38) Ma, M.; Zheng, S.; Chen, H.; Yao, M.; Zhang, K.; Jia, X.; Mou, J.; Xu, H.; Wu, R.; Shi, J. A Combined "RAFT" and "Graft From" Polymerization Strategy for Surface Modification of Mesoporous Silica Nanoparticles: Towards Enhanced Tumor Accumulation and Cancer Therapy Efficacy. *J. Mater. Chem. B* 2014, *2*, 5828−5836.

(39) Liang, B.; He, M. L.; Chan, C.; Chen, Y.; Li, X. P.; Li, Y.; Zheng, D.; Lin, M. C.; Kung, H. F.; Shuai, X. T.; Peng, Y. The Use of Folate-PEG-grafted-hybranched-PEI Nonviral Vector for the Inhibition of Glioma Growth in the Rat. *Biomaterials* 2009, *30*, 4014−4020.